Article

# Charge Transport Parameters of the Pentathienoacene Crystal

Eung-Gun Kim, Veaceslav Coropceanu, Nadine E. Gruhn, Roel S. Snchez-Carrera, Robert Snoeberger, Adam J. Matzger, and Jean-Luc Brdas

*J. Am. Chem. Soc.*, **2007**, 129 (43), 13072-13081• DOI: 10.1021/ja073587r • Publication Date (Web): 04 October 2007



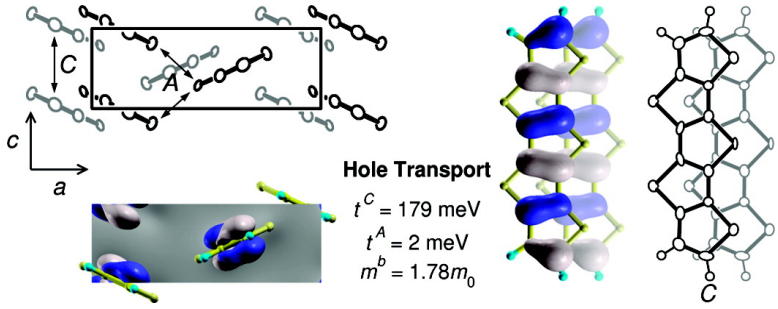


## More About This Article

Additional resources and features associated with this article are available within the HTML version:

- Supporting Information
- Links to the 10 articles that cite this article, as of the time of this article download
- Access to high resolution figures
- Links to articles and content related to this article
- Copyright permission to reproduce figures and/or text from this article

View the Full Text HTML

J|A|C|S
ARTICLES
Published on Web 10/04/2007

# Charge Transport Parameters of the Pentathienoacene Crystal

Eung-Gun Kim,[†] Veaceslav Coropceanu,[†] Nadine E. Gruhn,[‡] Roel S. Sánchez-Carrera,[†] Robert Snoeberger,[†,||] Adam J. Matzger,[§] and Jean-Luc Brédas*,[†]

*Contribution from the School of Chemistry and Biochemistry and Center for Organic Photonics and Electronics, Georgia Institute of Technology, Atlanta, Georgia 30332-0400, Department of Chemistry, University of Arizona, Tucson, Arizona 85721-0041, and Department of Chemistry and the Macromolecular Science and Engineering Program, University of Michigan, Ann Arbor, Michigan 48109-1055*

Received May 18, 2007; E-mail: jean-luc.bredas@chemistry.gatech.edu

***Abstract:*** Pentathienoacene, the thiophene equivalent of pentacene, is one of the latest additions to the family of organic crystal semiconductors with a great potential for use in thin film transistors. By using density functional theory and gas-phase ultraviolet photoelectron spectroscopy, we investigate the microscopic charge transport parameters of the pentathienoacene crystal. We find that the valence band exhibits a stronger dispersion than those in the pentacene and rubrene single crystals with marked uniaxial characteristics within the molecular layer due to the presence of one-dimensional $\pi$-stacks; a small hole effective mass is also found along the direction perpendicular to the molecular layers. In the conduction band, strong intermolecular sulfur−sulfur interactions give rise to a significant interstack electronic coupling whereas the intrastack dispersion is greatly reduced. The intramolecular vibronic coupling (reorganization energy) is stronger than that in pentacene but comparable to that in sexithiophene; it is larger for holes than for electrons, as a result of low-frequency modes induced by the sulfur atoms. The polarization energy is large, but its effect on the vibronic coupling remains small. Charge transport is discussed in the framework of both band and hopping models.

## 1. Introduction

Oligothiophenes and oligoacenes are two prototypical organic semiconductors actively pursued for use in thin film transistors (TFTs).[1−3] Well-defined crystal structures, combined with improved purification and film deposition techniques, have made these oligomers and their derivatives the most studied classes of organic semiconductors (see Scheme 1). Recent breakthroughs in solution processing that enable roll-to-roll printing now place small-molecule-based devices close to commercialization for low-cost, large-area electronic and optoelectronic applications.[4,5]

Efforts have been directed toward enhancing intramolecular $\pi$-conjugation in oligothiophenes by bridging adjacent $\beta$-carbon atoms with a sulfur linkage, thereby fusing the rings; this is the case, for example, in bisdithienothiophene (BDT: quaterthiophene with two bridges)[6] and oligothienoacenes ($n$TA: fully fused oligothiophenes).[7−11] The ring fusion can also be accompanied by changes in molecular packing, for instance, from

***Scheme 1.*** Chemical Structures of Actively Investigated $\pi$-Conjugated Organic Semiconductors[a]

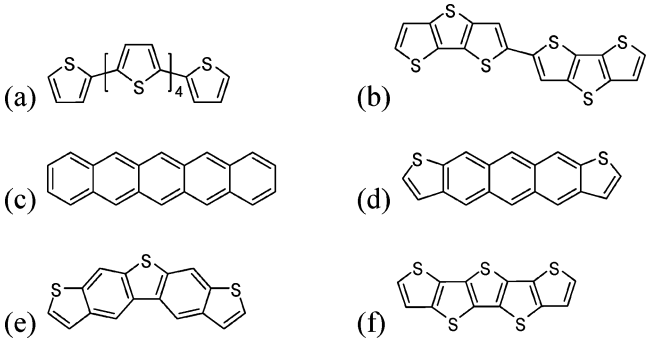


[a] (a) Sexithiophene (6T), (b) bisdithienothiophene (BDT), (c) pentacene, (d) *syn*-anthradithiophene (*syn*-ADT), (e) *syn*-thienobisbenzothiophene (*syn*-TBBT), and (f) pentathienoacene (5TA).

[†] Georgia Institute of Technology.
[‡] University of Arizona.
[§] University of Michigan.
[||] Current address: Department of Chemistry, Yale University, New Haven, CT 06520-8107.

(1) Katz, H. E. *J. Mater. Chem.* **1997**, *7*, 369−376.
(2) Horowitz, G. *Adv. Mater. (Weinheim, Ger.)* **1998**, *10*, 365−377.
(3) Dimitrakopoulos, C. D.; Malenfant, P. R. L. *Adv. Mater. (Weinheim, Ger.)* **2002**, *14*, 99−117.
(4) Mushrush, M.; Facchetti, A.; Lefenfeld, M.; Katz, H. E.; Marks, T. J. *J. Am. Chem. Soc.* **2003**, *125*, 9414−9423.
(5) Payne, M. M.; Parkin, S. R.; Anthony, J. E.; Kuo, C.-C.; Jackson, T. N. *J. Am. Chem. Soc.* **2005**, *127*, 4986−4987.
(6) Li, X.-C.; Sirringhaus, H.; Garnier, F.; Holmes, A. B.; Moratti, S. C.; Feeder, N.; Clegg, W.; Teat, S. J.; Friend, R. H. *J. Am. Chem. Soc.* **1998**, *120*, 2206−2207.
(7) Mazaki, Y.; Kobayashi, K. *Tetrahedron Lett.* **1989**, *30*, 3315−3318.
(8) Mazaki, Y.; Kobayashi, K. *J. Chem. Soc., Perkin Trans. 2* **1992**, 761−764.
(9) Sato, N.; Mazaki, Y.; Kobayashi, K.; Kobayashi, T. *J. Chem. Soc., Perkin Trans. 2* **1992**, 765−770.
(10) Zhang, X.; Côté, A. P.; Matzger, A. J. *J. Am. Chem. Soc.* **2005**, *127*, 10502−10503.


**10.1021/ja073587r CCC: $37.00** 

a less favorable herringbone packing to the desired $\pi$-stacking. Numerous attempts have also been made to overcome the shortcomings of pentacene, the five-ring member of the oligoacene family that presents among the highest hole mobilities for organic crystals.[12] These approaches include a functionalization of the molecular backbone with sulfur, as in anthradithiophene (ADT: the end benzene rings are replaced with a thiophene ring)[13,14] and thienobisbenzothiophene (TBBT: the central and two end rings are replaced);[15−17] these compounds display improved environmental stability and solubility as well as modified crystal packing. It is therefore no surprise that pentathienoacene (5TA), which can be viewed either as a thiophene equivalent of pentacene or as a fully fused terthiophene, has received special attention. It has recently become even more appealing, as new synthetic routes are now available[10,11] and 5TA-based TFTs have promising characteristics[11] (the thin-film field-effect mobility of 0.045 $cm^2/V$ s can be compared to the reported value of 0.02 $cm^2/V$ s for sexithiophene (6T)[18,19]).

In the present work, we investigate a series of oligothienoacenes with a focus on 5TA by using a joint theoretical−experimental approach that combines density functional theory (DFT) methods and high-resolution gas-phase ultraviolet photoelectron spectroscopy (UPS). In particular, we examine the electronic and vibronic coupling in these systems, which dictate the charge transport properties in the crystal.[20] This work provides the first in-depth molecular picture of the charge transport parameters in this potentially important family of thienoacene semiconductors.

## 2. Methodology

**2.1. Theoretical.** Geometry optimizations and normal mode calculations of isolated *n*TA molecules ($n = 3-7$) were performed at the B3LYP/6-31G(d,p) level using the Gaussian package.[21] The normal mode frequencies and Huang−Rhys factors were obtained with the DUSHIN code[22] and used to simulate the vibrational structure of the first ionization peak within the framework of the Born−Oppenheimer and Franck−Condon approximations according to the procedure described in detail elsewhere.[23] The frequencies were scaled down by a factor of 0.9613, which has been shown to reproduce the experimental IR frequencies very well.[24]

The calculations on the 5TA crystal were performed on an orthorhombic unit cell containing four molecules. The molecular coordinates determined by X-ray diffraction on the single crystal[10] were used with and without further geometry optimization (the cell constants were fixed at the experimental values during optimization). The wavefunctions were obtained using plane waves via a direct inversion in the iterative subspace (DIIS) method[25] at special *k*-points with a Monkhorst−Pack mesh[26] of $4 \times 2 \times 12$. The electronic band structure was constructed in a non-self-consistent manner from the optimized electron density with an iterative Lanczos diagonalization method.[27] The inverse effective mass tensor was calculated using Sperling's centered difference method at the band edges with $dk = 0.0017$ ($2\pi$/Bohr). Norm-conserving numerical pseudopotentials generated with the procedure of Troullier and Martins[28] were used for C and S, and a local analytic pseudopotential for H, with a plane-wave energy cutoff of 70 Ry. The plane wave DFT calculations reported here were carried out at the BLYP level with the CPMD (Car−Parrinello Molecular Dynamics) code.[29] In addition, the transfer integrals for nearest-neighbor pairs of molecules in the geometry-optimized crystal were calculated by using a fragment orbital approach[30] in combination with a basis set orthogonalization procedure.[31] We also computed the transfer integral for the diagonal pair in the 6T crystal[32] for comparison. These calculations were performed with the PW91 functional and Slater-type triple-$\zeta$ plus polarization (TZP) basis sets, using the ADF (Amsterdam Density Functional) package.[33]

**2.2. Experimental.** 5TA and 7TA were synthesized following the procedure of Zhang et al.[10] Both compounds were subsequently purified by sublimation ($(7.0-8.0) \times 10^{-5}$ Torr at 150−160 °C for the former and $(4.0-5.0) \times 10^{-5}$ Torr at 230−245 °C for the latter).

Gas-phase UPS spectra (He I) were recorded on an instrument built around a 36 cm radius, 8 cm gap hemispherical analyzer (McPherson, 10 cm gap) using a custom-designed photon source and collection methods. Instrument control and electron counting were provided by a National Instruments PCIe-6259 multifunction DAQ board and custom software. Samples were sublimed cleanly with no evidence of decomposition in the gas phase or as a solid residue. Sublimation temperatures, as monitored with a K-type thermocouple passed through a vacuum feed and attached directly to the ionization cell ($10^{-4}$ Torr), were 160−190 °C for 5TA and 280−330 °C for 7TA. The argon $^2P_{3/2}$ ionization at 15.759 eV was used as an internal calibration lock of the absolute ionization energy, and its difference with the $CH_3I$ $^2E_{1/2}$ ionization at 9.538 eV provided an external calibration of the energy scale. The instrument resolution (measured as the full width at half-maximum (fwhm) of the argon $^2P_{3/2}$ ionization) was 0.021−0.028 eV during data collection. The intensity of the spectra was corrected according to an experimentally determined analyzer sensitivity function. The He I spectra were also corrected for He I$\beta$ resonance line emission from the source, which is about 3% of the intensity of the He I$\alpha$ line emission and at 1.869 eV higher photon energy.

## 3. Results and Discussion

**3.1. Geometric Structure.** The optimized geometries of the isolated *n*TA molecules in the neutral state show that the C=C bonds lengthen and the C−C bonds shorten in going from the periphery to the center (see Figure 1, top panel for the C−C bonds). The gradual evolution of the bond lengths is still visible


(11) Xiao, K.; Liu, Y.; Qi, T.; Zhang, W.; Wang, F.; Gao, J.; Qiu, W.; Ma, Y.; Cui, G.; Chen, S.; Zhan, X.; Yu, G.; Qin, J.; Hu, W.; Zhu, D. *J. Am. Chem. Soc.* **2005**, *127*, 13281−13286.
(12) Goldmann, C.; Haas, S.; Krellner, C.; Pernstich, K. P.; Gundlach, D. J.; Batlogg, B. *J. Appl. Phys.* **2004**, *96*, 2080−2086.
(13) Laquindanum, J. G.; Katz, H. E.; Lovinger, A. J. *J. Am. Chem. Soc.* **1998**, *120*, 664−672.
(14) Kwon, O.; Coropceanu, V.; Gruhn, N. E.; Durivage, J. C.; Laquindanum, J. G.; Katz, H. E.; Cornil, J.; Brédas, J.-L. *J. Chem. Phys.* **2004**, *120*, 8186−8194.
(15) Wex, B.; Kaafarani, B. R.; Kirschbaum, K.; Neckers, D. C. *J. Org. Chem.* **2005**, *70*, 4502−4505.
(16) Coropceanu, V.; Kwon, O.; Wex, B.; Kaafarani, B. R.; Gruhn, N. E.; Durivage, J. C.; Neckers, D. C.; Brédas, J.-L. *Chem.—Eur. J.* **2006**, *12*, 2073−2080.
(17) Wex, B.; Kaafarani, B. R.; Schroeder, R.; Majewski, L. A.; Burckel, P.; Grell, M.; Neckers, D. C. *J. Mater. Chem.* **2006**, *16*, 1121−1124.
(18) Dodabalapur, A.; Torsi, L.; Katz, H. E. *Science* **1995**, *268*, 270−271.
(19) Torsi, L.; Dodabalapur, A.; Rothberg, L. J.; Fung, A. W. P.; Katz, H. E. *Science* **1996**, *272*, 1462−1464.
(20) Brédas, J.-L.; Beljonne, D.; Coropceanu, V.; Cornil, J. *Chem. Rev. (Washington, DC, U.S.)* **2004**, *104*, 4971−5003.
(21) Frisch, M. J., et al. *Gaussian 98*, revision A.11.1; Gaussian, Inc.: Pittsburgh, PA, 2001.
(22) Reimers, J. R. *J. Chem. Phys.* **2001**, *115*, 9103−9109.
(23) Malagoli, M.; Coropceanu, V.; da Silva Filho, D. A.; Brédas, J.-L. *J. Chem. Phys.* **2004**, *120*, 7490−7496.
(24) Wong, M. W. *Chem. Phys. Lett.* **1996**, *256*, 391−399.
(25) Hutter, J.; Lüthi, H. P.; Parrinello, M. *Comput. Mater. Sci.* **1994**, *2*, 244−248.
(26) Monkhorst, H. J.; Pack, J. D. *Phys. Rev. B* **1976**, *13*, 5188−5192.
(27) Pollard, W. T.; Friesner, R. A. *J. Chem. Phys.* **1993**, *99*, 6742−6750.
(28) Troullier, N.; Martins, J. L. *Phys. Rev. B* **1991**, *43*, 1993−2006.
(29) *CPMD*, 3.9.2; IBM Corp (Copyright 1990−2004) and Max-Planck Institut für Festkörperforschung Stuttgart (Copyright 1997−2001): 2005.
(30) Senthilkumar, K.; Grozema, F. C.; Bickelhaupt, F. M.; Siebbeles, L. D. A. *J. Chem. Phys.* **2003**, *119*, 9809−9817.
(31) Valeev, E. F.; Coropceanu, V.; da Silva Filho, D. A.; Salman, S.; Brédas, J.-L. *J. Am. Chem. Soc.* **2006**, *128*, 9882−9886.
(32) Siegrist, T.; Fleming, R. M.; Haddon, R. C.; Laudise, R. A.; Lovinger, A. J.; Katz, H. E.; Bridenbaugh, P.; Davis, D. D. *J. Mater. Res.* **1995**, *10*, 2170−2173.
(33) *ADF*, 2005.01; Scientific Computing and Modeling NV: Amsterdam, 2005.

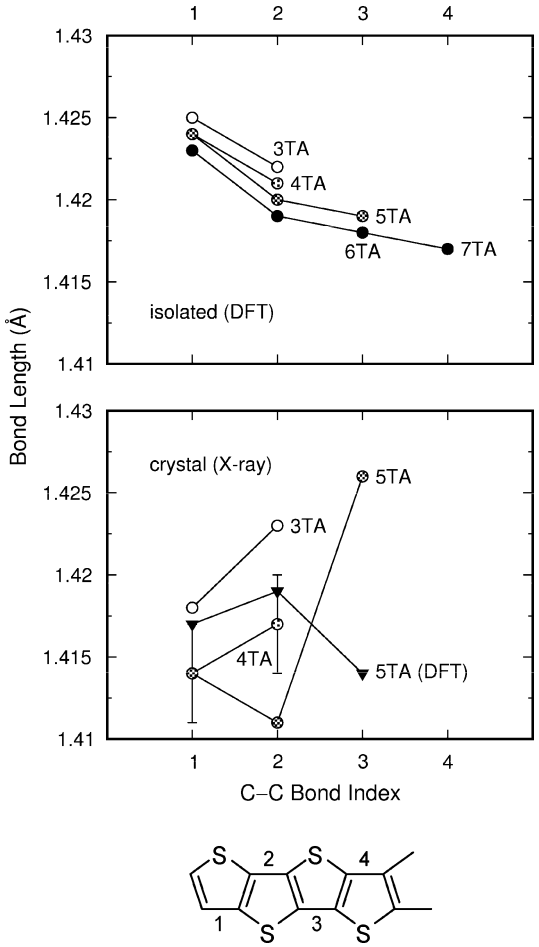


***Figure 1.*** Evolutions of the C−C bond lengths in going from the end to the center of the molecule: (top panel) DFT calculations on isolated molecules and (bottom panel) experimental crystal data. In the top panel, three data points of 6TA overlap with those of 7TA. In the bottom panel, DFT values are also given for the 5TA crystal.

all the way to the molecular center even in 7TA. On the other hand, the C−S bond lengths alternate and converge already at the fourth bond from the periphery. Similar trends are found in the experimental crystal structures of 3TA[34] and 4TA[8] for the C═C and C−S bonds.

The optimized molecular geometry of 5TA in the crystal indicates that the spatial evolution of the bond lengths remains unaffected by intermolecular interactions with the exception of the C−C bond lengths. The calculated C−C bond lengths increase sharply in the first inner thiophene ring before heading down to follow the evolution of the isolated case. The experimental crystal data, on the other hand, show the opposite trend (see Figure 1, bottom panel). We believe that this apparent discrepancy is due to the uncertainty in the X-ray data of 5TA as a result of polycrystallinity in the sample.[10] Indeed, the sharp increase in C−C bond length in going from the outer ring to the next is clearly seen experimentally in the better resolved crystal structures of 3TA[34] and 4TA;[8] the standard deviation there is less than 0.004 Å whereas it is as large as 0.02 Å (i.e., the full axis length in the figure) in the case of 5TA[10] (see also Figure 1, bottom panel). The trend calculated with DFT is also seen in the experimental crystal structures of TIPS-5TA and

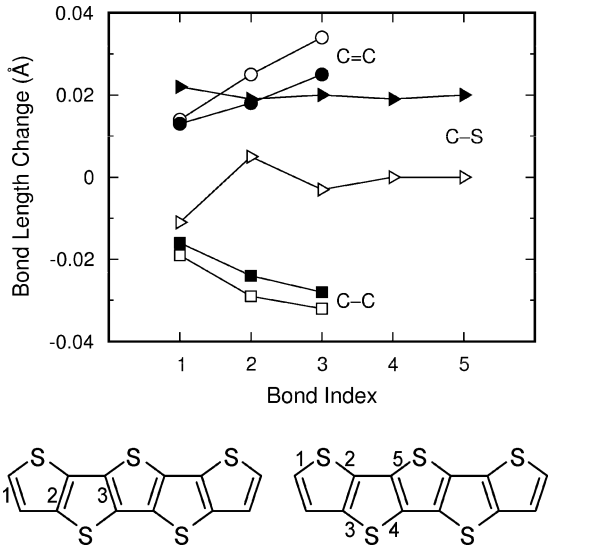


***Figure 2.*** Calculated bond length changes in isolated 5TA upon oxidation (open symbols) and reduction (filled symbols).

TIPS-7TA[10] (both ends are substituted by triisopropylsilyl groups at the α-positions). It is worth mentioning that, despite the inability of DFT to describe van der Waals interactions,[35] a number of studies have shown that constraining the lattice constants to experimental values effectively compensates the missing attractive interactions so that such DFT calculations reproduce not only the geometry of the molecules in the unit cell but also their pressure-dependent molecular orientation[36] and vibrational properties.[37,38]

We also note that (i) the geometry optimization of the 5TA crystal leads to a slight change in the stacking distance from 3.517 to 3.527 Å (both values are smaller than the experimental stacking distance of 3.576 Å for 4TA) and (ii) the crystal packing of 5TA is similar to that of α-terthiophene (3T)[39] in having a double-layered unit cell.

We now turn to the geometric relaxation upon oxidation or reduction of an isolated molecule (see Figure 2 for the case of 5TA). The C═C and C−C bonds undergo geometric changes to a greater extent in the cationic state than in the anionic state; the bond relaxations occur over the entire molecule and are more pronounced toward the molecular center. For the C−S bond, on the other hand, the geometric relaxations are more pronounced toward the molecular periphery and occur predominantly upon reduction (as we will see below in Figure 4, the wavefunctions of the highest occupied molecular orbital (HOMO) have nodes on the sulfur atoms); the weak geometric changes in the cationic state are localized to the molecular ends (1.5 thiophene rings at each end). The role of the sulfur atoms in transport will be discussed further when we examine the electronic structure and vibronic coupling in the following subsections.

**3.2. Molecular Electronic Structure.** Figure 3 shows the gas-phase UPS spectra of 5TA and 7TA. Those of *n*TA with *n*

(34) Bertinelli, F.; Palmieri, P.; Stremmenos, C.; Pelizzi, G.; Taliani, C. *J. Phys. Chem.* **1983**, *87*, 2317−2322.
(35) Zhao, Y.; Truhlar, D. G. *J. Chem. Theory Comput.* **2005**, *1*, 415−432.
(36) Hummer, K.; Puschnig, P.; Ambrosch-Draxl, C. *Phys. Rev. B* **2003**, *67*, 184105.
(37) Hermet, P.; Bantignies, J.-L.; Rahmani, A.; Sauvajol, J.-L.; Johnson, M. R.; Serein, F. *J. Phys. Chem. A* **2005**, *109*, 1684−1691.
(38) Kearley, G. J.; Johnson, M. R.; Tomkinson, J. *J. Chem. Phys.* **2006**, *124*, 044514.
(39) Van Bolhuis, F.; Wynberg, H.; Havinga, E. E.; Meijer, E. W.; Staring, E. G. J. *Synth. Met.* **1989**, *30*, 381−389.

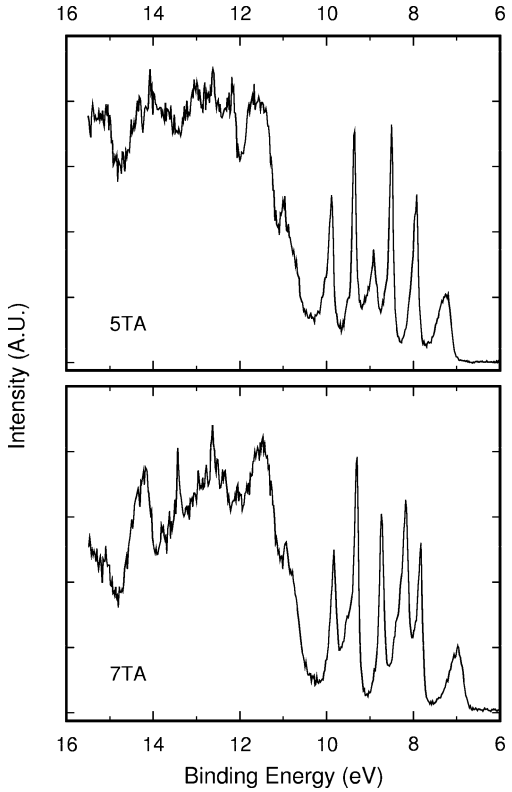


***Figure 3.*** Gas-phase UPS spectra of 5TA and 7TA.

***Table 1.*** Values of the First Ionization Energy for Isolated *n*TA Molecules as Calculated at the Koopmans Theorem and Self-Consistent Field (ΔSCF) Levels and Estimated from Gas-Phase UPS Spectra (Energies in eV)

| | Koopmans[a] | ΔSCF[b] | experiment |
|---|---|---|---|
| 3TA | 5.61 | 7.38 | 7.78[c] |
| 4TA | 5.43 | 7.02 | 7.52[c] |
| 5TA | 5.30 | 6.76 | 7.25[d] |
| 6TA | 5.21 | 6.56 | – |
| 7TA | 5.14 | 6.40 | 6.97[d] |

[a] Negative of the HOMO energy. [b] Vertical ionization energy. [c] From Sato et al.[9] [d] This work.

= 2, 3, 4 were previously reported by Sato et al.[9] The first ionization peak is located at 7.25 and 6.97 eV for 5TA and 7TA, respectively. The ionization energy of 5TA, as measured at the peak maximum, is significantly larger than that of pentacene (6.589 eV)[40] and nearly the same as that of 3T (7.38 eV).[41]

Our UPS data on 5TA and 7TA, together with those reported earlier on 3TA and 4TA,[9] show that the first ionization energy of *n*TA decreases with oligomer length (see Table 1), as in oligothiophenes[41] and oligoacenes.[42] The experimental oligomer length dependence of the ionization energy is well reproduced by the calculations at both the Koopmans theorem and self-consistent field levels, with the latter being in good quantitative agreement with experiment. The marked size dependences of the HOMO and lowest unoccupied molecular orbital (LUMO) energies translate the fact that the corresponding wavefunctions are fully delocalized along the long molecular axis (see Figure 4).

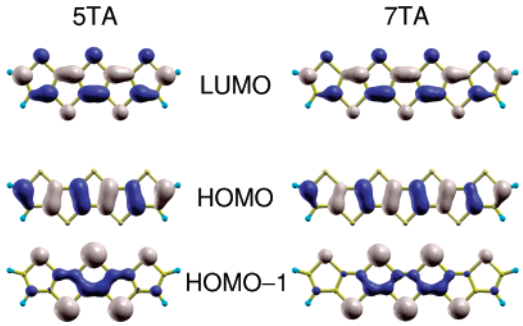


***Figure 4.*** Wavefunctions of the frontier molecular orbitals in isolated 5TA and 7TA.

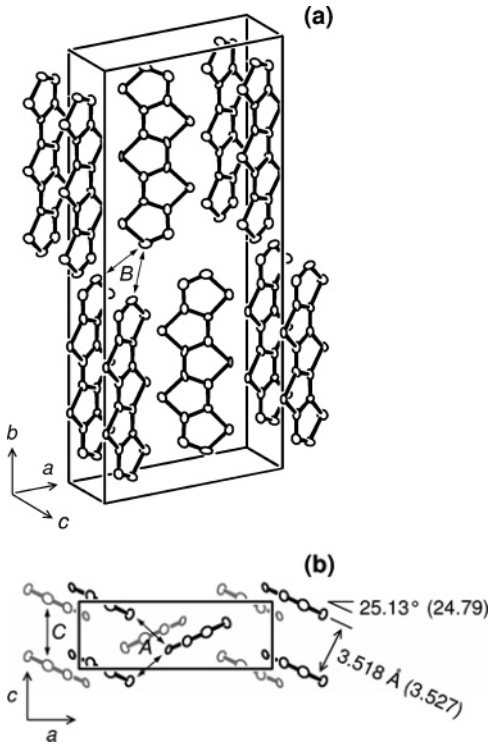


***Figure 5.*** Crystal structure of 5TA.[10] The experimental lattice constants of the orthorhombic unit cell (*Pnma*) are $a = 11.171$, $b = 25.098$, and $c = 3.8852$ Å. Shown in (b) is a view from the bottom along the *b*-axis, where the molecules in gray belong to the top layer of the double-layered unit cell. Rolled $\pi$-stacks (displaced along the short molecular axis) are clearly seen along the *c*-axis. Values in parentheses refer to the DFT-optimized structure. The nearest-neighbor pairs *A*, *B*, and *C* considered for calculation of the transfer integrals are indicated by arrows (note that the two arrows for each of the *A* and *B* pairs are not equivalent although their transfer integrals are nearly identical).

**3.3. Crystal Electronic Structure.** Figure 5 illustrates the X-ray crystal structure of 5TA obtained by Zhang et al.[10] A displacement of 1.650 Å [1.629 Å from DFT] along the short molecular axis (or a *roll* according to the terminology of Curtis et al.[43]) and a small stacking distance of 3.517 [3.527] Å are indicative of $\pi$-stacks along the *c*-axis. This one-dimensional $\pi$-stacking is in contrast to the herringbone packing found in pentacene. The "rolled" $\pi$-stacks in the 5TA crystal can be

(40) Coropceanu, V.; Malagoli, M.; da Silva Filho, D. A.; Gruhn, N. E.; Bill, T. G.; Brédas, J.-L. *Phys. Rev. Lett.* **2002**, *89*, 275503.
(41) da Silva Filho, D. A.; Coropceanu, V.; Fichou, D.; Gruhn, N. E.; Bill, T. G.; Gierschner, J.; Cornil, J.; Brédas, J.-L. *Philos. Trans. R. Soc. London, Ser. A* **2007**, *365*, 1435−1452.
(42) Sánchez-Carrera, R. S.; Coropceanu, V.; da Silva Filho, D. A.; Friedlein, R.; Osikowicz, W.; Murdey, R.; Suess, C.; Salaneck, W. R.; Brédas, J.-L. *J. Phys. Chem. B* **2006**, *110*, 18904−18911.
(43) Curtis, M. D.; Cao, J.; Kampf, J. W. *J. Am. Chem. Soc.* **2004**, *126*, 4318−4328.

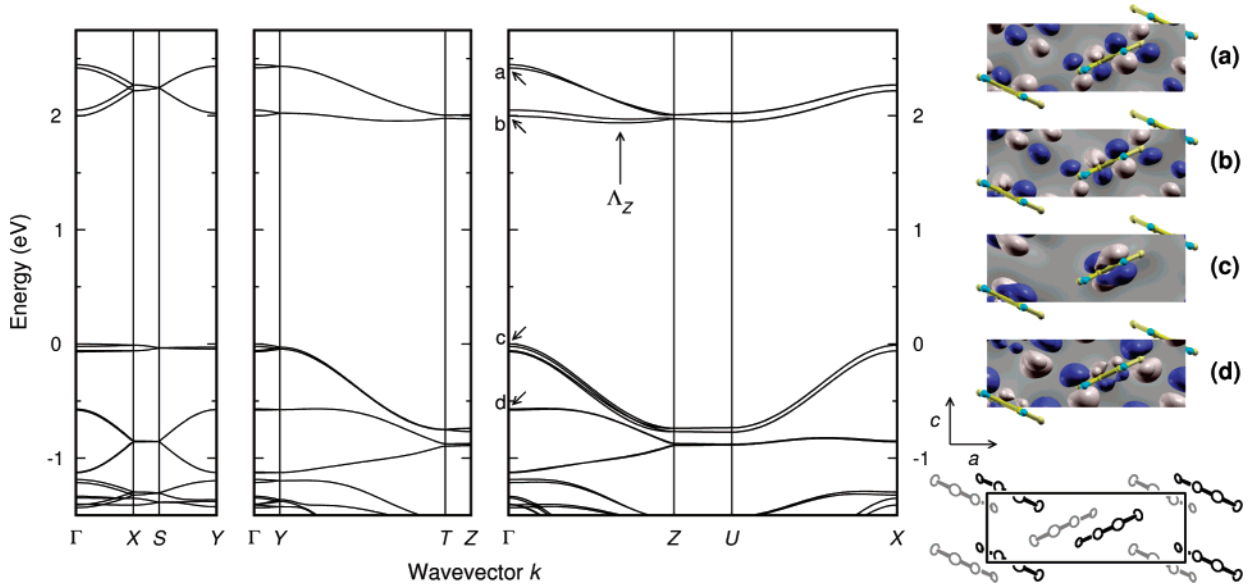


***Figure 6.*** Electronic band structure of the geometry-optimized 5TA crystal. Points of high symmetry in the first Brillouin zone are Γ = (0, 0, 0); *X* = (0.5, 0, 0); *Y* = (0, 0.5, 0); *Z* = (0, 0, 0.5); *S* = (0.5, 0.5, 0); *T* = (0, 0.5, 0.5); and *U* = (0.5, 0, 0.5), all in crystallographic coordinates. The energy levels are shifted such that the valence band edge at the Γ-point aligns at 0 eV. The conduction band edge denoted by $\Lambda_Z$ (0, 0, 0.337) is located 59 meV below the Γ-point. The wavefunctions of the crystal orbitals at the Γ-point (for the bottom molecular layer) are shown on the right, with each corresponding to a labeled arrow in the band structure plot.

compared to the "pitched" $\pi$-stacks found in the rubrene crystal[44] that also exhibits very high mobilities[45] (the *pitch* is defined by Curtis et al.[43] as the displacement along the long molecular axis). We note that the crystal unit cell of 5TA consists of four translationally inequivalent molecules.

The electronic band structure of the 5TA crystal is shown in Figure 6 along various orientations in reciprocal space. The valence band consists of four nearly degenerate $\pi$-subbands and has a width *W* of 0.77 eV. Importantly, when comparison is made among DFT results, this valence bandwidth is larger than that of pentacene[46,47] and almost twice as large as that of rubrene.[48] The strongest dispersion responsible for the large bandwidth is found along the *c*-axis (in the Γ*Z* section of the Brillouin zone), as expected from the $\pi$-stacking in this direction. A flat band is observed along the *a*-axis (Γ*X*); in rubrene, by contrast, a moderate dispersion was observed along the other inlayer crystal axis. A weakly dispersive band is found along the *b*-axis (Γ*Y*), that is, in the direction perpendicular to the molecular layers.

The quasi-degeneracy of the valence band indicates that interactions at the HOMO level among the translationally inequivalent molecules are very weak. This conclusion, obvious from the strong orientational anisotropy of the band dispersion, is also supported by direct calculations of the transfer integrals; among the three molecular pairs highlighted in Figure 5, a significant electronic coupling only occurs for pair *C*, i.e., along the *c*-axis (note that the nearest neighbors in pair *C* are translationally equivalent whereas those in pairs *A* and *B* are not). The transfer integral for pair *C*, $t_h^C$, is 179 meV, to be compared to $t_h^A = 2$ meV for pair *A* and $t_h^B = 6$ meV for pair *B*. The valence band can therefore be represented by a superposition of four weakly interacting subbands that are one-dimensional in character, and it is not surprising that the bandwidth from the band structure (0.77 eV) is in good agreement with the value derived from a one-dimensional tight-binding model ($4t_h^C = 0.72$ eV).

The very weak dispersion along the *a*-axis occurs despite the close proximity of the neighboring molecules; S...S distances in pair *A* are only ~3.55 Å, less than the sum of the van der Waals radii, whereas C...C distances are >4.9 Å. This is due to the presence of nodes on the sulfur atoms in the HOMO, which effectively decouples the HOMOs from one another along the *a*-axis (see Figure 6c for the crystal wavefunction of the topmost $\pi$-subband).

The conduction band, like the valence band, arises from the interactions of only one type of molecular orbitals, the LUMOs in this case. A reduced full bandwidth of 0.51 eV for the four subbands but with a significant subband splitting indicates that the pattern of electronic coupling is markedly different in the conduction states. (Actually, the *shape* of the conduction band is similar to that of the valence band; the notable difference is due to the strong subband splitting in the former.) As expected from the band dispersion in Γ*Z*, the transfer integral calculations give again the largest value for pair *C* ($t_e^C = 63$ meV); this value, however, is nearly three times as small as that for holes. The major reduction results from a mutual cancellation of bonding and antibonding interactions of the LUMO wavefunctions between the molecules in the pair (see Figure 7 for the interplay between the roll in the stack and the wavefunction pattern that changes, or does not change, phase across the short molecular axis).

Another feature, which is directly relevant to the subband splitting, is the significant electronic coupling between translationally inequivalent molecules along the *a*-axis, as manifested by the splitting in Γ*X*; the electronic coupling in pair *A* ($t_e^A =$

(44) Jurchescu, O. D.; Meetsma, A.; Palstra, T. T. M. *Acta Crystallogr., Sect. B* **2006**, *62*, 330−334.
(45) Podzorov, V.; Menard, E.; Borissov, A.; Kiryukhin, V.; Rogers, J. A.; Gershenson, M. E. *Phys. Rev. Lett.* **2004**, *93*, 086602.
(46) de Wijs, G. A.; Mattheus, C. C.; de Groot, R. A.; Palstra, T. T. M. *Synth. Met.* **2003**, *139*, 109−114.
(47) Hummer, K.; Ambrosch-Draxl, C. *Phys. Rev. B* **2005**, *72*, 205205.
(48) da Silva Filho, D. A.; Kim, E.-G.; Brédas, J.-L. *Adv. Mater. (Weinheim, Ger.)* **2005**, *17*, 1072−1076.

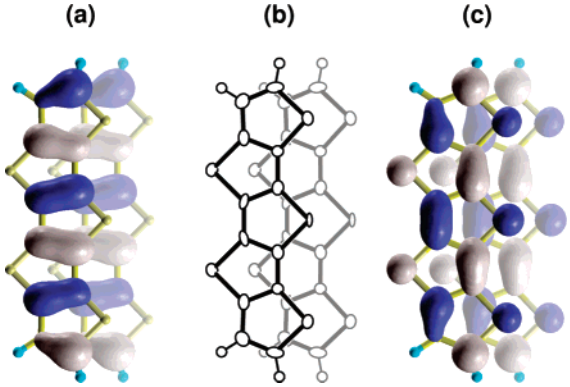


***Figure 7.*** Illustration of rolled $\pi$-stacking and of the HOMO and LUMO interaction patterns: (b) two adjacent molecules from the unit cell along the *c*-axis as viewed down the molecular plane normal; and (a) the HOMO and (c) LUMO wavefunctions of isolated 5TA from Figure 4 laid over each of the molecules in (b). The wavefunction overlap between the two molecules is significant; however, the LUMO electronic coupling is greatly reduced by the roll in the stack which, in combination with the alternating LUMO phase along the short molecular axis, creates both in-phase and out-of-phase interaction patterns.

42 meV) is now comparable to that in pair *C*. The difference in electronic interactions between the LUMO and HOMO levels for pair *A* can be explained by their charge density patterns; unlike the latter, the former carries a significant charge density on the sulfur atoms, which promotes effective electronic interactions through short S...S contacts spaced at about 3.55 Å (see Figure 4 and compare 6b and 6c). On the other hand, the electronic coupling between adjacent molecular layers (or in pair *B*) remains very small ($t_e^B = 7$ meV) and similar to that found for holes.

Importantly, the LUMO interactions along the *a*- and *c*-axes do not work in a constructive manner. That is, the splitting via pair *A* separates the subbands along $\Gamma Z$ at $\Gamma$, so that the top two subbands become more dispersive and the bottom two become less dispersive. As will be discussed below, it is the bottommost subbands that are of interest with regard to charge transport. We also note that the conduction band edge is shifted away from the zone boundary *Z* to $\Lambda_Z$ (0, 0, 0.337); the energy at $\Lambda_Z$ is 59 meV lower than that at $\Gamma$, making the states around $\Gamma$ less accessible (see Figure 6).

The theoretical derivation of the crystal properties requires, in general, an integration over the entire Brillouin zone. In the case of wide bands (or at low temperature), where the only populated states are those around the band edges, the description of many properties including charge transport can be simplified by using the effective mass approximation. The concept of the effective mass derives from the idea that an electron in a crystal can be treated as a free particle but with an *effective* mass that accounts for the effect of the periodic crystal potential.[49] The inverse effective mass $m_{ji}^{-1}$ is a tensorial quantity defined as[49]

$$m_{ji}^{-1} = \frac{1}{\hbar^2}\frac{\partial^2 \epsilon}{\partial k_j \partial k_i} \qquad (1)$$

where subscripts *i* and *j* denote the Cartesian coordinates in reciprocal space, $\epsilon$ the band energy, $\hbar$ the Planck constant, and *k* the electron momentum. Subsequent diagonalization of $m_{ji}^{-1}$ provides the principal components and their orientations.

(49) Seeger, K. *Semiconductor Physics: An Introduction*, 9th ed.; Springer-Verlag: Berlin, 2004.

***Table 2.*** Hole and Electron Effective Masses[a] $m_{ii}$ at the Band Edges in the Geometry-Optimized 5TA Crystal

| | $m_i/m_0$ | parallel to |
|---|---|---|
| holes at $\Gamma$ | 1.26 | *c* |
| | 1.78 | *b* |
| | 38.5 | *a* |
| electrons at $\Lambda_Z$ | 3.15 | *b* |
| | 7.46 | $a - 0.176c$ |
| | 8.26 | $0.021a + c$ |
| electrons at *U*[b] | 1.42 | *b* |
| | 4.44 | $0.133a + c$ |
| | 7.14 | $0.912a - c$ |
| electrons at $\Gamma$ | 1.01 | *a* |
| | 1.85 | *b* |
| | −10.8[c] | *c* |

[a] Taken from the diagonal components of the inverse effective mass tensors in principal axis coordinates and normalized by the free electron mass at rest $m_0$. [b] *U* located 10 meV above the conduction band edge $\Lambda_Z$. [c] The negative value reflects that the $\Gamma$-point is not a local energy minimum.

The calculated effective masses are reported in Table 2. Holes in 5TA are light with the smallest hole effective mass equal to $1.26m_0$, a value smaller than that in pentacene[46,47] (for comparison, the effective masses in silicon are $0.69m_0$ for a hole and $0.26m_0$ for an electron[50]). Electrons are much heavier than the holes; the smallest electron effective mass at the band edge is $3.15m_0$.

Interestingly, the effective mass displays a less pronounced orientational anisotropy than the band dispersion. That is, the hole effective mass along the *b*-axis ($1.78m_0$), despite the very flat band along this direction, is a mere 40% larger than that along the *c*-axis ($1.26m_0$). The unexpected hole behavior arises from the fact that the effective mass not only depends on the band dispersion but also scales with the unit cell dimensions in reciprocal space. This dependence can be illustrated by a one-dimensional tight-binding model, where the effective mass is given by[51]

$$m = \frac{\hbar^2}{2td^2} \qquad (2)$$

That is, the effective mass decreases linearly with the electronic coupling *t* and quadratically with the intermolecular distance (or cell length) *d*. Similar behavior can be expected for electrons, and the effect is more dramatic. At the conduction band edge and a higher energy valley at *U* (10 meV above the band edge), an electron attains the smallest effective mass along the *b*-axis.

**3.4. Vibronic Coupling.** In organic semiconductors, there are two major electron−phonon (vibration) coupling mechanisms that affect charge transport properties.[52,53] The first is referred to as local coupling and arises from the modulation of the site energy by intra- and intermolecular vibrations; it is the key interaction in Holstein's molecular crystal model.[54,55] The second mechanism is related to the modulation of the transfer

(50) Sze, S. M. *Semiconductor Devices: Physics and Technology*, 2nd ed.; John Wiley: New York, 2001.
(51) Kittel, C. *Quantum Theory of Solids*; Wiley: New York, 1963.
(52) Silinsh, E. A.; Čápek, V. *Organic Molecular Crystals: Interaction, Localization, and Transport Phenomena*, 2nd ed.; AIP Press: New York, 1994.
(53) Pope, M.; Swenberg, C. E. *Electronic Processes in Organic Crystals and Polymers*, 2nd ed.; Oxford University Press: New York, 1999.
(54) Holstein, T. *Ann. Phys. (N.Y., NY, U.S.)* **1959**, *8*, 325−342.
(55) Holstein, T. *Ann. Phys. (N.Y., NY, U.S.)* **1959**, *8*, 343−389.

***Table 3.*** Calculated Intramolecular Reorganization Energies for Hole ($\lambda_h$) and Electron ($\lambda_e$) Transfer in the *n*TA Series (Energies in meV)

| | $\lambda_h$ AP[a] (NM)[b] | $\lambda_e$ AP (NM) |
|---|---|---|
| 3TA | 352 (352) | 324 (325) |
| 4TA | 325 (325) | 293 (292) |
| 5TA | 306 (308) | 270 (270) |
| 6TA | 291 (292) | 252 (252) |
| 7TA | 279 (279) | 237 (237) |

[a] From adiabatic potential energy surfaces. [b] From normal mode analysis.

integral by intermolecular vibrations and referred to as nonlocal coupling; this electron−phonon coupling constitutes the main interaction considered in Peierls-type models.[56]

The strength of the local vibronic coupling is measured by the polaron binding energy $E_{pol}$ or, in the context of electron transfer theory, by the reorganization energy $\lambda$ ($\approx 2E_{pol}$). The reorganization energy consists of intra- and intermolecular contributions; the former reflects changes in the geometry of individual molecules, and the latter, changes in the location of the surrounding molecules, upon going from the neutral to the charged state and vice versa.

We first focus on the intramolecular contribution to $\lambda$. The intramolecular reorganization energy can be computed either from adiabatic potential energy surfaces or from normal mode calculations.[20] The results obtained by both approaches are collected in Table 3. The hole reorganization energy of 5TA is slightly larger than that of 6T (301 and 255 meV for the nonplanar and planar neutral geometries, respectively),[41] about twice as large as that of *syn*-TBBT (148 meV),[16] and three times as large as that of pentacene (97 meV).[40] 5TA, like 6T, shows a stronger vibronic coupling for holes than for electrons, in contrast to TBBT and pentacene.

It has been shown[40,57] for a number of aromatic compounds that the strength of vibronic coupling scales as the inverse of the number of $\pi$-electrons $N$. As shown in Figure 8, *n*TA closely follows the $1/N$ relationship,[58] provided that $\pi$-electrons are counted differently depending on the carrier type: for hole transfer, only $\pi$-electrons on carbon atoms are considered whereas two $\pi$-electrons per sulfur atom are also added for electron transfer (this is again due to the different wavefunction patterns of the frontier orbitals with regard to sulfur). The

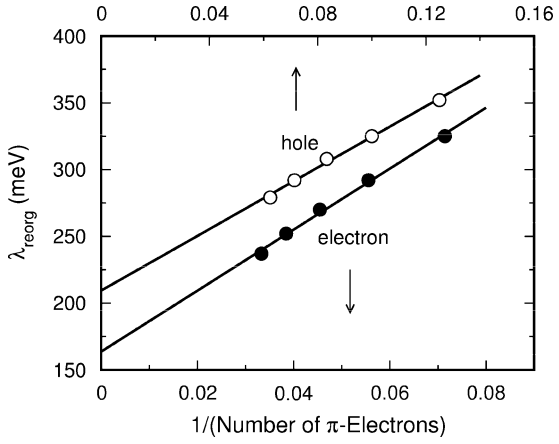


***Figure 8.*** Hole− and electron−vibration coupling, as represented by the reorganization energy $\lambda_{reorg}$, as a function of the number of relevant $\pi$-electrons $N$. Straight lines are fits to $1/N$.

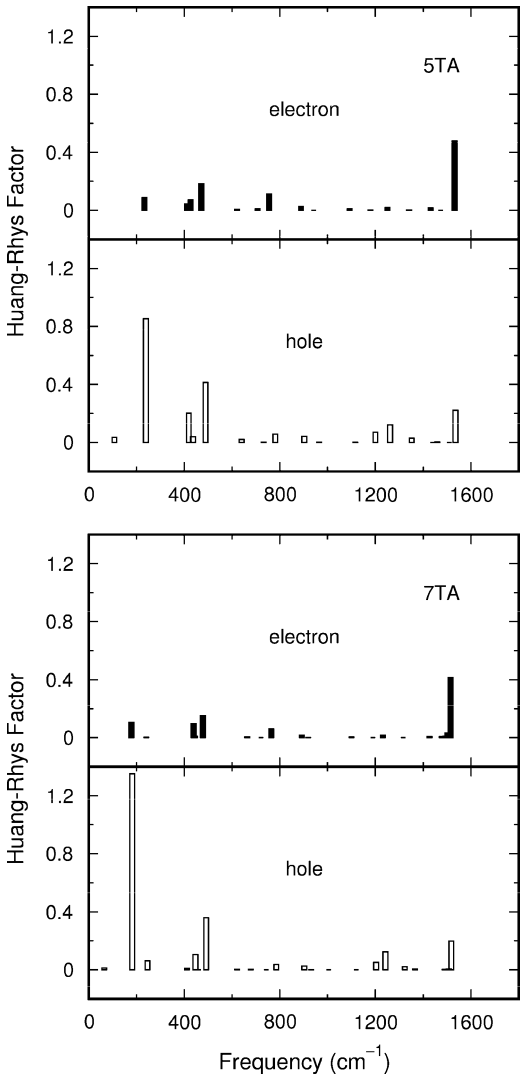


***Figure 9.*** Huang−Rhys factors $S_i$ of 5TA and 7TA. The relaxation energy $\lambda_i$ contributed by each normal mode at frequency $\omega_i$ is obtained by $\lambda_i = \hbar\omega_i S_i$.

vibronic coupling shows a stronger dependence on the number of $\pi$-electrons for electrons than for holes. The reorganization energy for the hypothetical polythienoacene, estimated from the fit, would approach 209 and 164 meV for hole and electron transfer, respectively. Interestingly, the same kind of extrapolation in the case of polyacene led to smaller and very similar values (~50 meV) for both holes and electrons.[40]

Decomposition of the intramolecular reorganization energy into individual contributions from the relevant vibrational modes shows that large values of the Huang−Rhys factor for hole transfer are found mostly at low frequencies (see Figure 9). In fact, 41% of the relaxation energy in 5TA (44% in 7TA) originates from low-frequency modes below 500 cm$^{-1}$ (~2.5 times the thermal energy). This is in marked contrast to the pentacene case, where there is almost no contribution from low-frequency vibrations.[23]

For electron transfer, on the other hand, 73% [78% for 7TA] of the total relaxation involves vibrational modes at about 1200

(56) Peierls, R. E. *Quantum Theory of Solids*; Oxford University Press: New York, 2001.
(57) Devos, A.; Lannoo, M. *Phys. Rev. B* **1998**, *58*, 8236−8239.
(58) As far as fitting is concerned, the size dependences are represented far better by a power law.

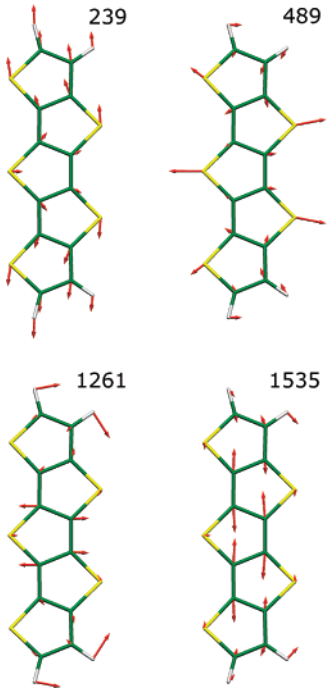


***Figure 10.*** Normal modes with strong vibronic coupling in cationic 5TA. The low-frequency modes at 239 and 489 $cm^{-1}$ involve mostly sulfur atoms, whereas the high-frequency modes at 1261 and 1535 $cm^{-1}$ involve carbon atoms. All modes are in-plane.

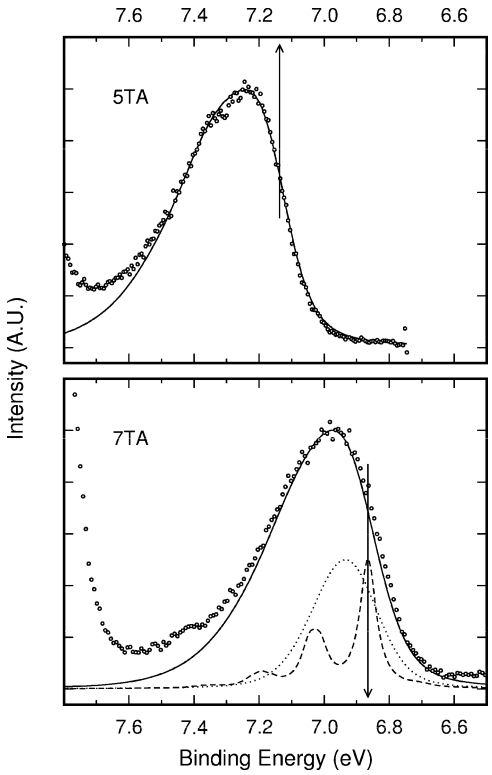


***Figure 11.*** Simulated first ionization peaks with the vibrational structure. Also shown are the close-up views of the experimental UPS spectra (open circles). The arrows indicate the experimental adiabatic ionization energies as obtained from the simulation (7.14 eV for 5TA and 6.87 eV for 7TA). The dashed and dotted curves were obtained by keeping only the high (>1200 $cm^{-1}$) and low frequencies (<500 $cm^{-1}$), respectively, without changing the parameters used for the full simulation (solid curve); the peak intensities in the partial simulations are reduced by half for clarity. The simulation temperature was 448 K for 5TA and 578 K for 7TA. Transition intensities were convolved with a Lorentzian function with fwhm = 0.06 eV.

$cm^{-1}$ or higher, and less than 7% [7%] comes from modes below 500 $cm^{-1}$. A similarly large contribution of high-frequency vibrations was found in TBBTs (over 70%);[16] the corresponding value in pentacene is about 61%.[14]

Further comparison of 5TA with TBBTs[16] indicates that the low-frequency vibronic coupling for holes grows with increasing sulfur content, although in TBBTs the low-frequency coupling is not strong enough to effect a larger reorganization energy for holes than for electrons. The most strongly coupled modes are illustrated in Figure 10. The 239 $cm^{-1}$ mode is characterized by C−S−C bending in the three inner thiophene rings, which leads to a stretching motion of the 5TA cation as a whole along the long molecular axis (the two outer rings move more or less as a rigid body). The 489 $cm^{-1}$ mode stretches the molecule along the short axis via C−S−C bending in the inner rings. The high-frequency modes with strong vibronic coupling for holes involve carbon atoms only. The 1261 $cm^{-1}$ mode consists of C=C stretching in the central ring (and two adjacent rings in the case of 7TA), and the 1535 $cm^{-1}$ mode represents C−C stretching within the three inner rings. The latter mode is also found in the 5TA anion at 1531 $cm^{-1}$ and provides the largest Huang−Rhys factor.

It has recently been shown[42] that the DFT estimates of the reorganization energy depend significantly on the amount of "exact" Hartree−Fock exchange included in the hybrid functionals. Among the standard functionals, B3LYP provides the best description of relaxation processes in oligoacenes. However, even B3LYP calculations can underestimate the Huang−Rhys factors to some extent. The simulations of the line shape of the first ionization peak in 5TA and 7TA (see Figure 11) underline that good agreement with experiment is obtained only when the B3LYP estimates of the Huang−Rhys factors are increased by 20−30%. Therefore, the reorganization energies given in Table 3 are considered to represent lower limits.

The simulations of the first ionization peak in 5TA and 7TA point to adiabatic ionization energies (or 0−0 transitions) located about 0.11 eV below the peak maxima (see Figure 11). This is in marked contrast to the case of oligoacenes, in which the adiabatic ionization energy coincides with the peak maximum.[23] The dominant low-frequency modes in 5TA and 7TA are responsible for the enhanced intensities at higher energies (see Figure 11, bottom panel for the curve simulated with low frequencies only).

When a hole (or an electron) is localized on a given molecule, its energy is modified by the electronic polarization $P_+$ that results from the interaction of the excess charge with both permanent and induced multipoles in the surrounding molecules. Coupling with phonons takes place through changes in $P_+$ as a result of intermolecular geometric relaxation. The relaxation energy from electronic polarization, $\Delta E_p$, can be estimated roughly by $\Delta E_p \sim P_+ \Delta d/d$, where $d$ and $\Delta d$ are the average distance and displacement, respectively, to the nearest-neighbor molecules.[52] $P_+$ can be obtained from the difference in UPS ionization energy between the gas and solid phases.[59]

Using the UPS data from Sato et al.[9] for the solid state, we estimate $P_+$ for 5TA to be 2.3 eV. This value is similar to that

(59) Sato, N.; Seki, K.; Inokuchi, H. *J. Chem. Soc., Faraday Trans. 2* **1981**, *77*, 1621−1633.

of 4TA (2.4 eV)[9] but larger than those of 3TA (1.6 eV),[9] 6T (1.6 eV),[41,60,61] and pentacene (1.7 eV).[59] The significantly larger values of $P_+$ for 5TA and 4TA are attributed to a particular packing pattern realized in these crystals, where intermolecular S...S distances are very small. For $\Delta d/d = 0.0125$ (the $\Delta d$ value of 0.05 Å used here may be compared to the largest displacement of 0.04 Å in the anthracene crystal calculated with force fields[62]), the reorganization energy due to polarization ($2\Delta E_p$) is therefore calculated to be about 60 meV for 5TA, which only adds a small contribution compared to the intramolecular reorganization energy. $2\Delta E_p$ for 6T, which has a slightly smaller intramolecular reorganization energy,[41] is calculated to be 40 meV at the same $\Delta d/d$. Taking into account a possible underestimation of the intramolecular reorganization energy by DFT (increased by 30%) and assuming similar polarization effects for electrons, we expect the total reorganization energy to be somewhere around 460 meV for holes and 410 meV for electrons.

A systematic investigation of nonlocal coupling would require knowledge of the full phonon dispersion spectra. To obtain a rough estimate of the nonlocal contribution to the overall vibronic coupling, we resort to recent combined quantum chemistry and molecular dynamics studies,[63−65] in which the degree of thermal fluctuations in transfer integral is seen not to exceed about 50 and 20 meV for pentacene and 6T, respectively, at 300 K. Comparing the pentacene and 6T results suggests that the nonlocal part becomes less important when the local part is large as found in 5TA.

**3.5. Bandlike vs Hopping Transport.** Despite several attempts to develop microscopic models based on the Holstein−Peierls Hamiltonian,[66−70] the current description of charge transport in molecular crystals remains incomplete (we note that the experimental determination of charge carrier mobilities is a very difficult task in its own right, as they are influenced by many factors such as disorder, impurities, temperature, electric field, and carrier density[71]). Therefore, we limit our discussion to two limiting transport regimes, namely, the band and hopping regimes.

According to band theory, the carrier mobility in wide bands is given by[49]

$$\mu = \frac{q\tau}{m} \tag{3}$$

where $q$ is the charge, $\tau$ the mean free time between collisions (or the mean relaxation time of the band state), and $m$ the effective mass of the charge carrier. The charge moves coherently in a wavelike manner and is scattered (or relaxed) by phonons from one momentum state to another. In the isotropic relaxation time approximation, the mobility and its orientational anisotropy are dictated by the effective mass.

Using eq 3 and the effective masses from Table 2, we expect that the hole mobility of 5TA is two-dimensional in the *bc*-plane with the highest along the *c*-axis and the lowest along the *b*-axis. The hole mobility of 5TA is greater than that of pentacene, if we assume that both have the same $\tau$. The fact that the mobility plane is perpendicular to the molecular layer may have implications for TFT applications. The intrinsic hole mobility may be much greater than the reported value of 0.045 $cm^2/V$ s measured on thin films on the *a*-$SiO_2$ surface, in which the molecular layer is parallel to the substrate[11] and thus the conduction is an average over the randomly oriented *c*-axes of individual grains. The orientation of the molecular layer relative to the substrate depends on the substrate material and/or deposition method (good such examples include pentacene on Ag[72] and graphite,[73] in which the molecular layer is perpendicular to the substrate). Therefore, growing a thin film of 5TA with the *bc*-plane, instead of the *ac*-plane, parallel to the substrate could improve the field-effect mobility, which would then correspond to an average of biaxial grain mobilities. We also note that the unusually large value for an interlayer hole mobility (over 70% of the highest mobility) may have implications for photovoltaics, in which charge transport perpendicular to the molecular layer could be crucial.[74]

The complex behavior of the conduction band allows no easy prediction for the electrons in the band regime. There are additional energy levels close to the conduction band edge (*U* and Γ, which can be populated even at moderate temperature). And for each energy level there exist different numbers of valleys (for instance, $\Lambda_Z$ has two equivalent valleys whereas Γ has one) and different orientational anisotropies associated with them. All these contributions are to be taken into account to calculate the overall or conductivity effective mass tensor, which would be beyond the scope of our study. However, it seems reasonable to conclude that the electron mobility is uniaxial along the *b*-axis. The highest electron mobility found perpendicular to the transport direction of TFTs may explain, at least partly, the experimental observation of p-channel-only field-effect behavior.[11]

When vibronic coupling becomes comparable to or stronger than electronic coupling, bandlike transport is expected to take place only in perfectly ordered systems at very low temperature. Increasing temperature gradually reduces the bandwidth, leading to an increase in effective mass and subsequently to localization of the charge. Motion of the charge carrier can then be modeled by a sequence of uncorrelated hops.[54,55] The hopping transport can be described as a self-exchange electron transfer from a charged (and relaxed) molecule to a nearby neutral molecule. The carrier mobility is expressed as[53]

$$\mu = \frac{qd^2}{k_B T} k_{ET} \tag{4}$$

where $k_B$ is the Boltzmann constant, $T$ the temperature, and $k_{ET}$ the electron transfer rate. At high temperature, the electron

(60) Telesca, R.; Bolink, H.; Yunoki, S.; Hadziioannou, G.; Van Duijnen, P. T.; Snijders, J. G.; Jonkman, H. T.; Sawatzky, G. A. *Phys. Rev. B* **2001**, *63*, 155112.
(61) Lögdlund, M.; Dannetun, P.; Fredriksson, C.; Salaneck, W. R.; Brédas, J.-L. *Phys. Rev. B* **1996**, *53*, 16327−16333.
(62) Brovchenko, I. V. *Chem. Phys. Lett.* **1997**, *278*, 355−359.
(63) Troisi, A.; Orlandi, G.; Anthony, J. E. *Chem. Mater.* **2005**, *17*, 5024−5031.
(64) Troisi, A.; Orlandi, G. *J. Phys. Chem. A* **2006**, *110*, 4065−4070.
(65) Troisi, A. *Mol. Simul.* **2006**, *32*, 707−716.
(66) Gosar, P.; Choi, S.-I. *Phys. Rev.* **1966**, *150*, 529−538.
(67) Munn, R. W.; Silbey, R. *J. Chem. Phys.* **1985**, *83*, 1843−1853.
(68) Munn, R. W.; Silbey, R. *J. Chem. Phys.* **1985**, *83*, 1854−1864.
(69) Hannewald, K.; Stojanović, V. M.; Schellekens, J. M. T.; Bobbert, P. A.; Kresse, G.; Hafner, J. *Phys. Rev. B* **2004**, *69*, 075211.
(70) Hannewald, K.; Bobbert, P. A. *Appl. Phys. Lett.* **2004**, *85*, 1535−1537.
(71) Coropceanu, V.; Cornil, J.; da Silva Filho, D. A.; Olivier, Y.; Silbey, R.; Brédas, J.-L. *Chem. Rev. (Washington, DC, U.S.)* **2007**, *107*, 926−952.
(72) Casalis, L.; Danisman, M. F.; Nickel, B.; Bracco, G.; Toccoli, T.; Iannotta, S.; Scoles, G. *Phys. Rev. Lett.* **2003**, *90*, 206101.
(73) Koch, N.; Vollmer, A.; Salzmann, I.; Nickel, B.; Weiss, H.; Rabe, J. P. *Phys. Rev. Lett.* **2006**, *96*, 156803.
(74) Yoo, S.; Domercq, B.; Kippelen, B. *Appl. Phys. Lett.* **2004**, *85*, 5427−5429.

transfer or hopping rate takes its semiclassical form of Marcus theory given by[53]

$$k_{ET} = A \exp\left[-\frac{(\lambda - 2t)^2}{4\lambda k_B T}\right] \quad (5)$$

The prefactor $A$ depends on the strength of electronic coupling: in the case of weak coupling (nonadiabatic regime), $A \sim t^2$; and in the case of strong coupling (adiabatic regime), $A$ is equal to the frequency of the nuclear motion along the reaction coordinate.

In the hopping regime, the hole mobility of 5TA becomes uniaxial along the *c*-axis; the large transfer integral leads to a negligibly small activation energy barrier of less than 10 meV ($t = 179$ and $\lambda = 460$ meV). The other two axes are close to the classical limit for weak electronic coupling with an energy barrier ($\approx \lambda/4$) of 110 meV. It is obvious from eqs 4 and 5 that the $d^2$ dependence that helped produce a light charge carrier perpendicular to the molecular layers along the *b*-axis in the band regime no longer plays a significant role. The highest hole mobility is expected to be greater than that of 6T, the energy barrier of which is estimated to be 60 meV ($t = 35$ and $\lambda = 370$ meV).

The hopping model predicts the electron mobility to be much smaller than the hole mobility. The largest electron mobility is found along the *c*-axis with an energy barrier of 50 meV, and the next along the *a*-axis (70 meV). The interlayer electron mobility, which is the most pronounced in the band regime, is here negligibly small with an energy barrier of 100 meV.

## 4. Conclusions

The key molecular parameters governing charge transport in the 5TA crystal have been identified by using DFT calculations complemented by gas-phase UPS. The main results can be summarized as follows. The 5TA crystal presents

(1) an exceptionally strong dispersion in the valence band ($W = 0.77$ eV, $t = 179$ meV, $m = 1.26m_0$) due to one-dimensional $\pi$-stacks;

(2) a much reduced dispersion in the conduction band ($W = 0.51$ eV, $t = 63$ meV) due to cancellation of bonding and antibonding interactions by the roll in the $\pi$-stacks;

(3) a significant electronic coupling between $\pi$-stacks in the conduction band ($t = 42$ meV) via intermolecular S...S interactions;

(4) a very small hole effective mass ($1.78m_0$) in the direction perpendicular to the molecular layers;

(5) large intramolecular reorganization energies;

(6) a larger intramolecular reorganization energy for holes (306 meV) than for electrons (270 meV) due to low-frequency vibrations induced by sulfur atoms; and

(7) a large electronic polarization energy (2.3 eV) due to short intermolecular S...S distances, although its role in local electron−phonon coupling is minor.

This study provides the first in-depth molecular picture of the structure−transport property relationships in the 5TA crystal. Interestingly, the transport parameters calculated here in the context of both the band and hopping models suggest that the *intrinsic* hole mobility in the 5TA crystal might be higher than that in two benchmark high-mobility organic crystals in their representative transport regimes: larger than pentacene in the band regime and larger than 6T in the hopping regime.

**Acknowledgment.** We thank Michael L. Blumenfeld for performing UPS measurements and Demétrio A. da Silva Filho and Karin Schmidt for stimulating discussions. This work was partly supported by the Office of Naval Research and the National Science Foundation under the STC (DMR-0120967) and CRIF (CHE-0443564) programs. Computational resources were partly provided by the Artic Region Supercomputing Center in Fairbanks, Alaska (ONRDC17403171).

**Supporting Information Available:** Complete ref 21. This material is available free of charge via the Internet at http://pubs.acs.org.

JA073587R